3D-Printed Polymer-Based Conformal Space Radiation Shield with Heat Dissipation

Yue Xiao[1], An Zou[2], David Carlson[3],
Advanced Cooling Technologies, Inc. Lancaster, PA 17601

Aminur Rahman[4], *and* Pu Zhang[5]
Department of Mechanical Engineering, The State University of New York at Binghamton, Binghamton, NY 13902

With the rapid development of SmallSats/CubeSats and space computing, the current aluminum (Al) bulk shielding technology poses challenges in Size, Weight, and Power (SWaP) requirements. The bulk shielding thickness is determined by the electronics with the least radiation resistance, which prohibits wider adoption of Commercial-off-the-shelf (COTS) electronics and results in increased system weight. In addition, the absence of advanced thermal management technologies for SmallSats/CubeSats largely limits the adoption of high-power, low-price, and readily available COTS electronics. To address these challenges, we developed an innovative 3D-printed, lightweight polymer composite radiation shield comprising a Fiber Reinforced Polymer Composite (FRPC) layer that is compatible with other polymer-based radiation shielding composites. Specifically, the FRPC utilizes aligned carbon fibers in the same base polymer to achieve high in-plane thermal conductivity for electronics heat dissipation. In addition, such a shield is manufactured by the advanced five-axis Direct Ink Writing (DIW) 3D printer for further improved thermal transport and structural strength. Further, the 3D-printed shield enables locally enhanced spot shielding to provide additional radiation shielding for sensitive electronics without increasing the overall shield thickness. For FRPC, we achieved 2.55 W/m-K in-plane thermal conductivity, which is ~4x higher than the base polymer. Overall, the shield prototype can achieve a 7 °C reduction in CPU temperature or a 22.5% increase in CPU power.

Nomenclature

k	=	thermal conductivity
k_{in}	=	in-plane thermal conductivity
A	=	sample area
T	=	temperature
x	=	thermal probe location

I. Introduction

SPACE radiation is one of the most important issues in the design of space systems. To protect electronics from damage caused by radiation effects, the mainstream space companies currently still adopt conventional bulk shielding techniques (Figure 2), where the printed electronic boards (PCBs) and electronics are enclosed in shielding boxes made of aluminum (Al), tungsten (W) alloys, etc. Although they provide satisfactory shielding performance, the high size, weight, and power (SWaP) requirements make them less ideal for SmallSats, CubeSats, and other space systems where the payload and volume are at a premium. In addition, the bulk shielding technique lacks the flexibility to accommodate electronics with lower radiation resistance, particularly for commercial-off-the-shelf (COTS)

[1] R&D Lead Engineer, 1046 New Holland Ave. Lancaster, PA 17601, yue.xiao@1-act.com
[2] R&D Engineer III, 1046 New Holland Ave. Lancaster, PA 17601, an.zou@1-act.com
[3] R&D Technician III, 1046 New Holland Ave. Lancaster, PA 17601, david.carlson@1-act.com
[4] Graduate Student, 4400 Vestal Pkwy E, Binghamton, NY 13902, arahma51@binghamton.edu
[5] Assistant Professor, 4400 Vestal Pkwy E, Binghamton, NY 13902, pzhang@binghamton.edu

Copyright © 2024 Advanced Cooling Technologies, Inc.

electronics that have higher performance and lower cost but are more prone to radiation damage. Moreover, the bulk shield itself provides limited thermal management of the PCB and electronics. In the current design, the heat generated by chips is transferred through the PCB to the heat sink, and additional radiators are required for high-power electronics. The additional thermal management system can further drive up the SWaP requirements on the system level.

To improve the radiation resistance, polymer composite material is a promising approach for its enhanced attenuation enabled by high-atomic-number (Z) metal elements or the strategically designed Z-gradient additives to the base polymer.[1] We have previously developed a Metal Oxide Polymer Composite (MOPC) that has ~700% higher mass attenuation coefficient for gamma ray at 123–247 keV energy range.[2] Based on the existing progress on polymer composite, an additional layer of Fiber Reinforced Polymer Composite (FRPC) that has a high in-plane thermal conductivity can be added between the MOPC and the space electronics for increased heat dissipation. The entire layered shielding material can be 3D printed to achieve conformal and locally enhanced radiation shielding to reduce the overall system weight (Figure 1).

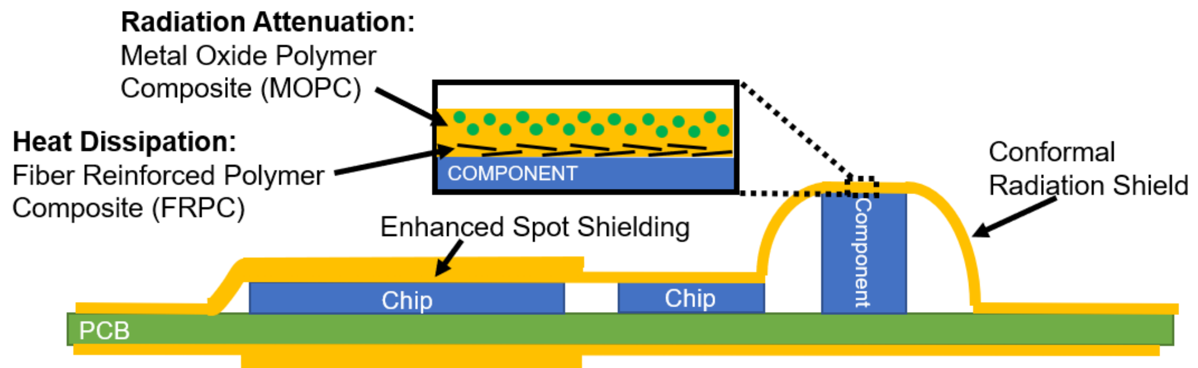

Figure 1. Space radiation shield comprising of MOPC and FRPC.

In polymers, the heat is carried by scattering sites, such as pervasive defects and structural disorders, leading to a low thermal conductivity on the order of 0.1 W/m-K or lower.[3] One common mechanism to enhance thermal conductivity is to load a polymer matrix with high thermal conductivity micro- or nano-fillers to form FRPC. In this case, the directional thermal conductivity can be significantly increased if the alignment of the filler matches the heat conduction direction. In addition, for fibrous fillers, a bridging material can be employed to interconnect individual fibers. As a result, the thermal resistance between fibers can be minimized to further increase the in-plane thermal conductivity and subsequently spread the heat from the heat-generating electronics to the area with lower temperatures or heat sink. Essentially, the FRPC creates an additional heat conduction path in addition to the existing PCB. Additionally, the large contact area between the chip and the FRPC further reduces the thermal resistance. Furthermore, the FRPC and MOPC share the same base polymer so minimum delaminating can be expected.

Additionally, to achieve improved heat spreading, a high in-plane thermal conductivity k_{in} is preferred, which requires the fiber alignment to become parallel to the heat flow direction. Studies have shown that for Direct Ink Writing (DIW) 3D printing technologies, the fiber additives can be automatically aligned with the printing direction benefitting from the extrusion flow under the sharing force, enabling an anisotropic thermal conductivity between the direction along and across the printing direction.[4] However, the conventional bottom-to-top 3-axis 3D printing technology, where curvatures are built layer-by-layer, suffers from additional thermal resistance due to the reduced area between layers, additional contact resistance, and most importantly, the fiber alignment is perpendicular to the heat flow (Figure 2). To resolve this issue, advanced 5-axis 3D printing systems need to be adopted to print curvature in a continuous printing path, instead of the multi-layer structure in 3-axis printing, so that the fibers can be aligned with the heat flow direction. Additionally, the continuous fiber is also expected to improve the mechanical strength of the FRPC.

With the material design and the manufacturing technology, we report a new space radiation shield design that features an FRPC layer for enhanced heat dissipation. Particularly, the FRPC layer utilizes carbon fibers and bridging materials to form a complete heat conduction path within the layer of FRPC to significantly increase k_{in} and subsequently reduce the electronics' hot spot temperature. Such an FRPC can be printed alone or along with the radiation-resistance MOPC to form a dual-purpose radiation shielding system.

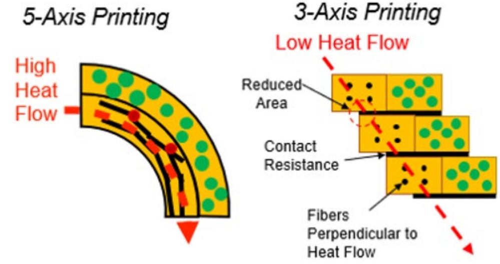

Figure 2. Comparison between 5-axis and 3-axis 3D printing technologies on fabricating FRPC and maximizing in-plane thermal conductivity.

II. Materials and Methods

A. FRPC material design and synthesis

In this work, a wide range of heat conduction fillers has been investigated, including alumina, silica, boron nitride, graphite, carbon nanotubes, carbon fibers, etc.[5] Among these materials, we selected carbon fibers due to their low cost, and more importantly, their potentially high thermal conductivity along the fiber direction. Particularly for DIW AM systems, the fibers would automatically align to the direction parallel to the nozzle extrusion direction due to the shear force during the extrusion.[4] Such a fiber alignment is difficult to achieve for cast polymer compositions.

For the bridging material, copper particles were employed to form a continuous heat conduction path in FRPC (Figure 3). Here we selected copper particles for their lower cost and high thermal conductivity. Due to the overall low vol. % of copper particles, the FRPC will not become conductive. Other materials such as graphene nanoplatelets (GNPs), graphene, and graphene oxide (GO) are also suitable bridging materials.

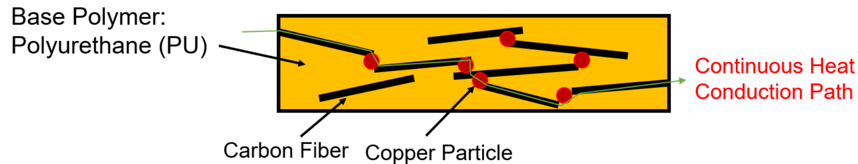

Figure 3. FRPC design. *Carbon fibers with high thermal conductivity are aligned and connected by copper particles to form a continuous heat conduction path for enhanced thermal conductivity of FRPC.*

With multiple fillers, the FRPC feedstock recipe development process for the DIW AM process can be complicated. DIW was selected to utilize the shear force at the sidewall of the printing nozzle to automatically align the carbon fibers to maximize in-plane thermal conductivity. Additionally, the viscosity of the feedstock must be high enough to maintain the shape after printing, but not too high to clog the printing nozzle. In this work, we identified that a third filler, nanoclay (NC) is an ideal candidate to improve the resin flow behavior during the printing process, i.e., crosslinking reaction and shear thinning property, so that the feedstock is suitable for 3D printing. Using NC, one typical recipe of the FRPC feedstock is Carbon Fiber: PU: Cu: NC (% v: v: v: v) = 20: 80: 10: 15. For this recipe, the carbon fiber has 16 vol. %, or 15 wt. %. In detail, carbon fibers (Asbury Carbons Inc.) with 7–9 µm in diameter and ~80 µm in length, Copper particles (US Research Nanomaterials, Inc.) with <20 µm in diameter, and NC (Sigma-Aldrich) with 30–70 µm in diameter and 1–3 µm in length were adopted.

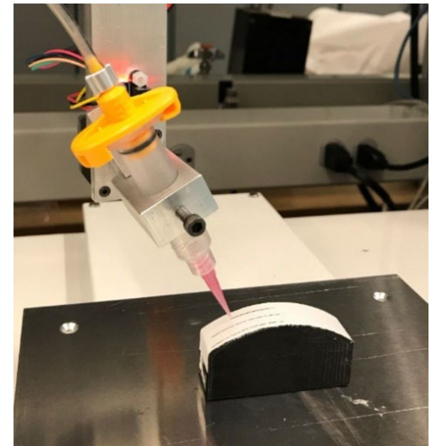

Figure 4. 5-axis 3D printing setup.

B. 5-axis DIW 3D Printing

A home-built 5-axis 3D printing system based on an existing 5-axis platform (JR-3304, Jarome, Figure 4) and slicing and path-planning techniques for various curved surfaces were developed. The platform can print a 400 mm x 400 mm area, which is much larger than the typical 1U PCB. The FRPC feedstock supply and extrusion system can be driven by a pneumatic pump or a stepper motor set coupled with screws and plungers.

C. Thermal conductivity measurements

As the thermal conductivity is improved by the alignment of the carbon fibers, the thermal conductivity of FRPC is expected to be anisotropic, thus popular and easy thermal conductivity measurement methods, i.e., laser flash, are not suitable for FRPC. Thus, a thermal conductivity measurement setup based on ASTM-E1530-11 was built (Figure 5). In this method, the tested sample was sandwiched between two reference blocks made of stainless steel. One block in contact with an aluminum plate with an embedded heater serves as a heat source, while the other in contact with a cold plate serves as the heat sink. Three thermocouples were used for each reference block to measure its temperature gradient, and two thermocouples were inserted into the sample for temperature gradient in the sample. Foams were wrapped around the reference blocks and the sample to minimize heat loss and ensure a one-direction heat path. With this setup, the thermal conductivity of the sample can be determined by

$$k_s = k_{ref} \cdot \frac{A_{ref} \cdot \frac{dT}{dx_{ref}}}{A_s \cdot \frac{dT}{dx_s}}, \tag{1a}$$

in which

$$\frac{dT}{dx_s} = \frac{T_4 - T_5}{\Delta x_s}, \quad \frac{dT}{dx_{ref}} = \frac{3T_1 - 4T_2 + T_3}{2\,\Delta x_{ref}}. \tag{1b}$$

Here k and A are the thermal conductivity and cross-sectional area, respectively. Subscript s and ref represent sample and reference blocks, respectively. In Eq. 1b, symbol Δx_s and Δx_{ref} are the distance between two thermocouples in the sample, and the distance between the evenly distributed thermocouples in the reference block, respectively. For each measurement, the temperature of the cooling fluid was fixed at 5 °C using a chiller, while the heater temperature is controlled by a temperature controller so that the sample is at room temperature (~25 °C). Before the measurement of the FRPC, the thermal conductivity measurement setup was first calibrated using a SS 316L sample with its thermal conductivity (~16.6 W/m-K) measured by the laser flash method. The SS 316 sample is longer than the FRPC sample for comparable thermal conductance. As a result, the measured thermal conductivity of SS 316L sample is 16.1 W/m-K, well within the 5% error. The heat loss through the foam is also at minimum, indicated by the <5% temperature difference between $T_1 - T_2$ and $T_2 - T_3$.

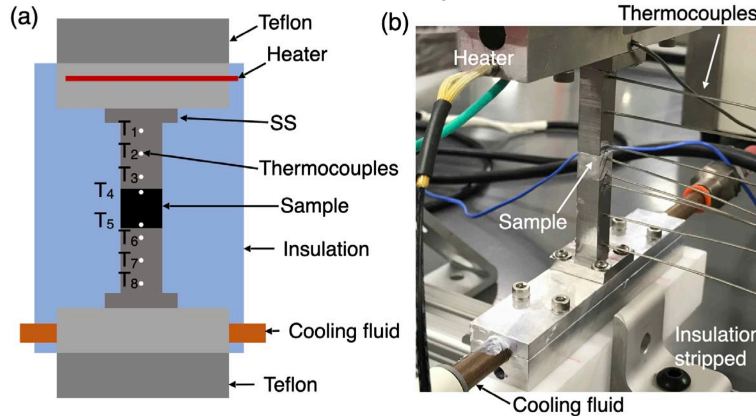

Figure 5. Thermal conductivity measurement setup. *(a) Schematic and (b) picture of the thermal conductivity measurement setup (insulation was stripped in b for the picture).*

III. Results and Discussion

A. 3D Printed FRPC sample

FRPC 3D printing was carried out after the determination of the feedstock recipe. Both large FRPC slabs (7 cm × 6 cm) and cubes (2.5 cm × 2.5 cm × 1.5 cm) were successfully printed with minimum bubbles in the samples (Figure 17), indicating suitable applications in space. Particularly, Figure 18a shows well-aligned carbon fibers in the printing direction in a 3D printed sample, whereas the carbon fibers were randomly orientated in a cast sample shown in Figure 18b. The alignment of the carbon fibers also contributes to superior structural strength.

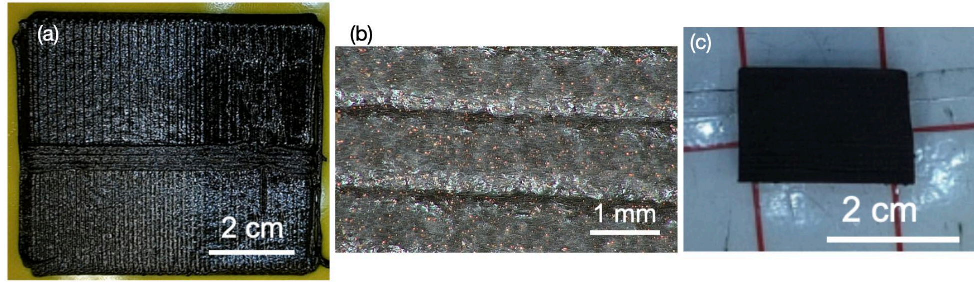

Figure 6. 3D-printed FRPC. *(a) The Top-down view and (b) the microscopic view of the 3D-printed slab. (c) The top-down view of the 3D-printed FRPC cube.*

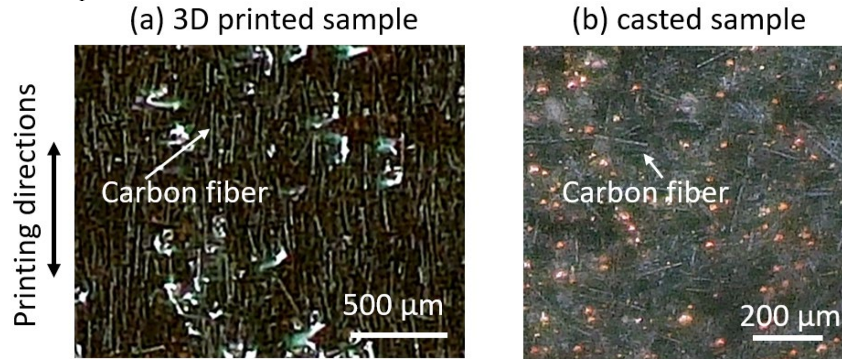

Figure 7. (a) 3D-printed and (b) cast FRPC sample. *The carbon fibers are well aligned in the 3D printed sample but only randomly oriented in the cast sample.*

B. Thermal conductivity and anisotropy

Figure 8a shows the results of the thermal conductivity of FRPC. Three samples are included: (i) PU1 with 16 vol. % (15 wt. %) of carbon fibers, (ii) PU2 with 16 vol. % (15 wt. %) of carbon fibers, and (iii) PU2 with 19 vol. % (18 wt. %) of carbon fibers. It is worth noting that the resin and hardener in PU1 and PU2 are the same chemicals but with different mixing ratios. The volume ratios of resin to hardener are 1:1 and 2:3 in PU1 and PU2 respectively. For each recipe, the thermal conductivity of the cast samples, and the in-plane direction and cross-plane direction of 3D printed samples were measured. The highest thermal conductivity was achieved by the recipe PU2 with 18 wt. % (19 vol.%) of carbon fibers. Compared to pure PU (0.68 W/m-K), the thermal conductivity of the cast sample, where carbon fibers are randomly oriented, is enhanced by 90%, while the in-plane thermal conductivity is enhanced by ~4× to 2.55 W/m-K, implying the effects of carbon fiber alignment on thermal conductivity. Compared to the values reported in recent publications,[6–11] 2.55 W/m-K of thermal conductivity is one of the highest values with lower carbon fiber wt. % (Figure 8b). The thermal conductivity of FRPC can be further improved by increasing the carbon fiber weight percentage, coating fillers (carbon fibers, copper particles, etc.) with a silicon dioxide layer, and adding other dopants, such as graphene oxide nanosheets.

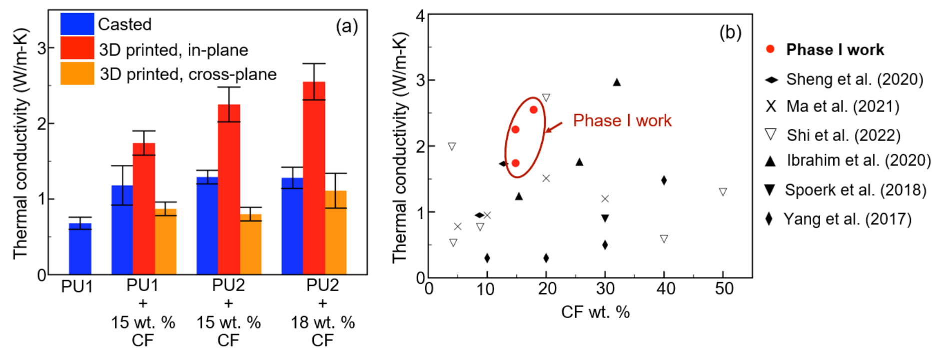

Figure 8. Thermal measurements. *(a) Directional thermal conductivity of FRPC. (b) Thermal conductivity comparison of FRPC between our work and previous works by Sheng et al.,[6] Ma et al.,[7] Shi et al.,[8] Ibrahim et al.,[9] Spoerk et al.,[10] and Yang et al.[11] CF: Carbon fiber.*

It is worth noticing that the FRPC is not designed to replace with the classical Al housing or a copper cold finger for high power electronics cooling. The FRPC is much lighter (~1.5 g/cm^3) and easy to deploy although the thermal conductivity is low. In this case, the FRPC is a heat spreading material to dissipate heat from the high-power electronics to the colder areas of the PCB and the heat sink.

C. 5-axis 3D printing

To produce higher stiffness and tougher structures such as a dome, the fiber orientation was designed in three different ways: layer A, layer B, and layer C. The fiber distribution in each type is theoretically different from each other such as 0°, and 90° with respect to the X-axis for layer A and layer B. Figure 9 illustrates that type ABAB comprised of both layer A and layer B in alternating order, which was only made possible with our five-axis AM systems. For conventional three-axis AM systems, type CCCC which contains all layer C was the only approach to fabricate such dome structures. As fiber distribution in ABAB is more oriented and alternating compared to the circular orientation of CCCC, potentially ABAB will deliver better structural strength.

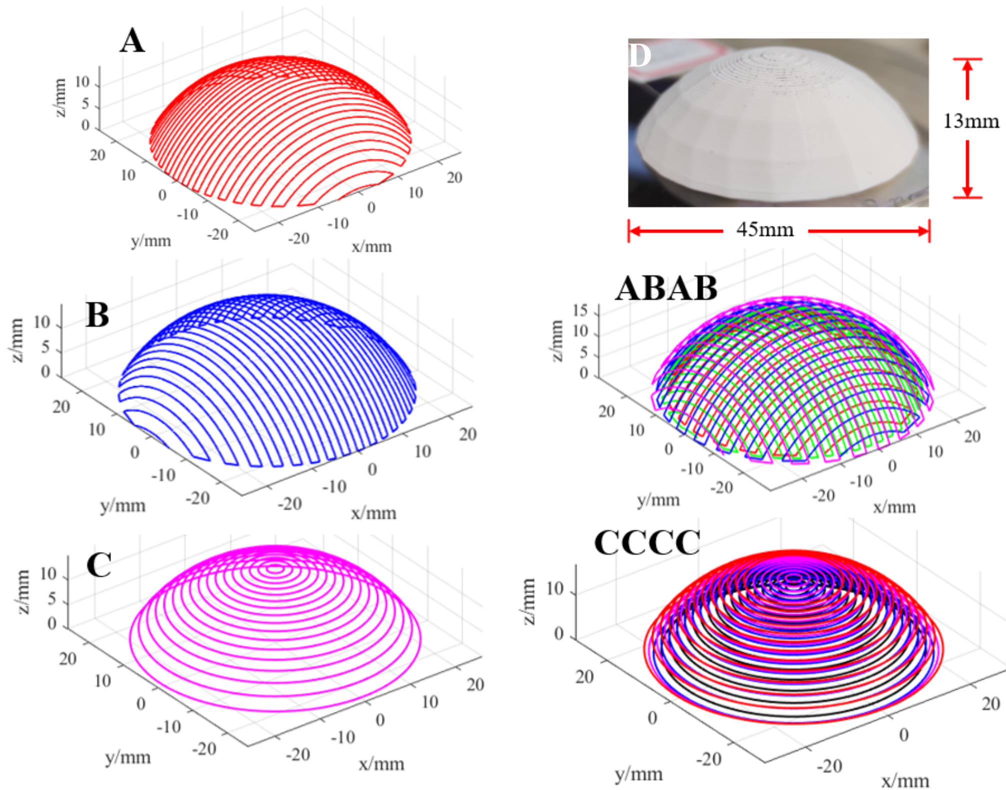

Figure 9. 3D printing path for a five-axis printer to produce dome-shaped samples with 45 mm ×13 mm dimension. *In type A, the fiber direction is 0° to the X-axis. In type B, fiber is oriented 90º to the X axis. In type C, fiber is oriented circularly. Type ABAB is stacked respectively in the order of layer A, layer B, layer A, and layer B. Type CCCC consists of only layer C. ABAB is only achievable via five-axis AM systems whereas conventional three-axis AM systems can only achieve CCCC.*

There are other parameters for the printing process such as pneumatic dispensing pressure, printing speed, curing time, needle type, and diameter for direct ink writing. Our optimal printing parameters so far are 10 mm/s printing speed and 30–40 bar dispensing pressure. Furthermore, to print the required samples, we used a tapered plastic needle of 610 µm diameter. The printing process is shown in Figure 10a. Type ABAB and CCCC both have 4 layers on top of each other, where the needle runs in a zigzag manner for type ABAB with the needle perpendicular to the printing paths and a circular manner for type CCCC. Figure 10b shows the printed sample using ABAB layers. Along another line, samples with CCCC layers (Figure 10c) were also fabricated for structural strength comparison, and Figure 10d

shows the inner surface of the sample. It is worth noticing that both samples have smooth surface finishes, and the samples remained undeformed during the printing process.

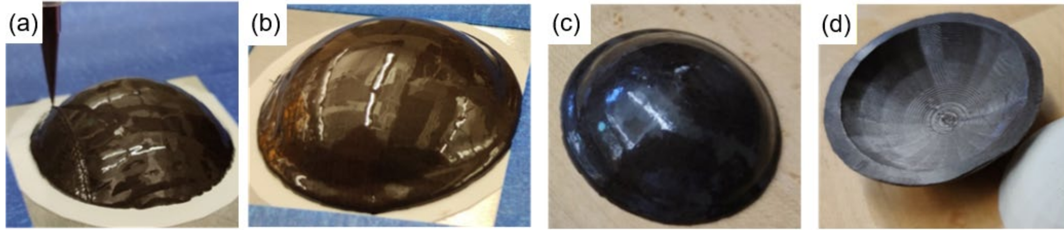

Figure 10. Printed dome. *(a) The 3D printing process of ABAB layers. (b) 3D printed dome with ABAB layers. (c) 3D printed dome with CCCC layers. (d) The bottom face of the 3D-printed dome.*

The printed domes were then tested using a load frame (ADMET eXpert 4000) to compare their structural strength (Figure 11a). It is clear from Figure 11b that the ABAB sample, fabricated by five-axis AM systems, has a maximum load of 42.29 N, and the CCCC sample, fabricated by three-axis AM systems, has only 30.65 N. The peak force of the ABAB sample is 40% higher than that of the CCCC sample. At the same time, the ABAB sample (five-axis printing) has a nearly 100% increase in stiffness compared to planner surface printing (three-axis printing). It indicates that for the ABAB sample, carbon fibers are aligned to the direction of printing and contributed to the reinforcement of structure by improving the stiffness. Certainly, the carbon fiber reinforcement effect is not contributing to the CCCC sample and therefore shows lower peak force and higher displacement. It is worth noticing that after releasing the force, both samples sprung back almost to the original shape, which is also an indication of having good elastic behavior.

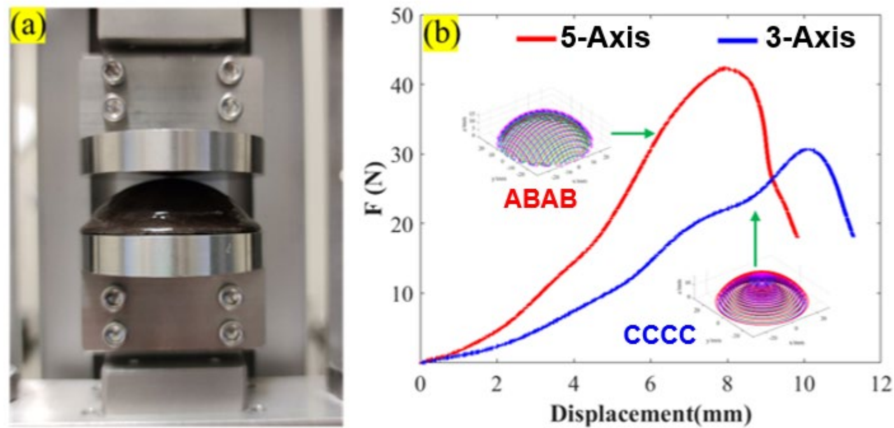

Figure 11. Compression test results of 3D printed dome-shaped samples. *(a) Compression test setup loaded with a sample. (b) Force-displacement curves of ABAB and CCCC domes. Compared to flat surface printing (CCCC), samples fabricated by curved surface printing (ABAB) have a 100% increase in stiffness and a 40% increase in peak forces.*

D. Prototype testing

After the initial validation on curved surfaces, a shield prototype (3 mm thick FRPC + 2 mm thick MOPC) designed for was fabricated and installed on a Raspberry PI (model 2 B) that served as the testing electronics (Figure 12a). The shield was built by a DIW system with nozzle diameter of 0.5 mm. In this case, 6 and 4 layers were printed for FRPC and MOPC, respectively. The entire printing process was completed within 0.5 h, which is less than the 50 min pot life of the base PU at room temperature. Overall the printing size is limited by the pot life of the polymer resin. For industrial applications, the nozzle and the resin temperature can be tuned to extend the overall printing window.

The MOPC is a variation of a previously reported polymer composite design, where Gd_2O_3 was adopted for its electron radiation attenuation capabilities.[12] Here the Raspberry PI is selected for its moderate size, representative PCB design with height differences across the board, and easy monitoring of CPU power and junction temperature. To promote thermal contact, a thin layer of vacuum grease was applied between the shield prototype and the CPU (heat

source) on Raspberry PI. Figure 12b presents the raspberry with the proposed shield on the top side. The Raspberry PI was fixed with four threaded rods on the heat sink.

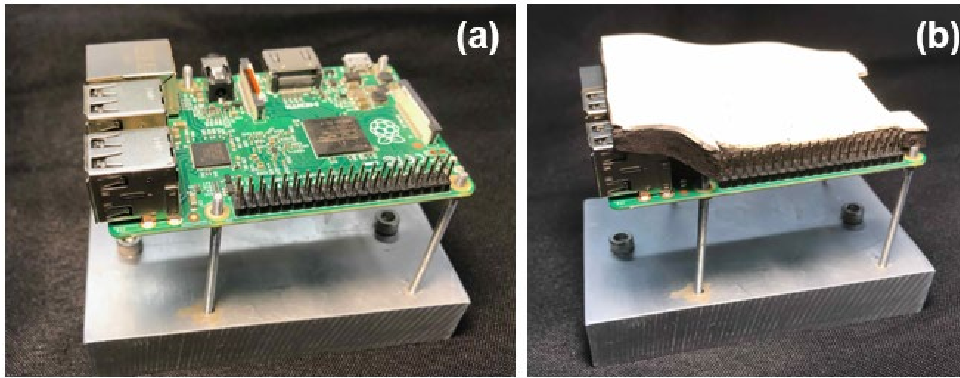

Figure 12. Shield installation on Raspberry PI. *(a) a Raspberry PI without the prototype shield fixed on the heat sink via four threaded rods. (b) The Raspberry PI is covered by the prototype shield. Raspberry PI dimensions: 8.5 cm × 5.6 cm × 2.0 cm.*

With the shield prototype deployed, we performed thermal performance tests in a vacuum environment. In these tests, the Raspberry PI was operated in a vacuum chamber with feedthrough for cooling fluid tubing, power cable, and data/power cable (Figure 13). The Raspberry PI was cooled by the cold plate, of which the temperature was regulated by a chiller circulating cooling fluid at 15 °C. The Raspberry PI was first run using a computing stress testing program at 99% - 100% CPU usage. The CPU frequency and junction temperature (hottest spot) can be directly extracted from the operation system, fundamentally eliminating the potential inconsistency induced by using external thermocouples. Raspberry PI has a built-in diode, of which the electrical current can be measured to extract the junction temperature. Although the absolute value of such extracted temperature may require further calibration, it is adequate to provide temperature information if compared against itself. The CPU frequency and junction temperature were recorded every 10 seconds until reaching a steady state where the temperature fluctuations with 3 min is < 1 K. Same tests were performed on the same Raspberry PI with and without the prototype shield, and the results are presented in Figure 14. For both cases, the CPU can operate at the maximum frequency (900 MHz), indicating that the CPU has not reached its thermal throttling temperature. It was first observed that the Raspberry PI with the shield is 7 °C lower in CPU junction temperature compared with that without the shield, indicating the additional benefit in thermal management enabled by the FRPC layer. Particularly, the lower junction temperature at the same frequency means that the electronics have the additional thermal budget to operate at higher power density, which is critical to space computing.

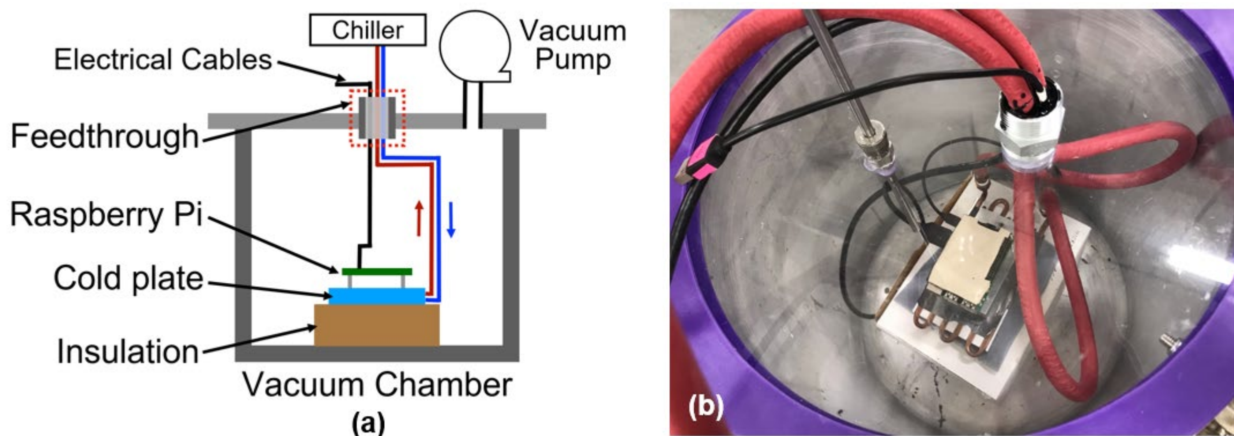

Figure 13. Prototype testing of the radiation shield. *(a) Schematic thermal testing of Raspberry PI covered by a prototype shield. (b) Picture of tested Raspberry PI in a vacuum chamber with the prototype shield installed.*

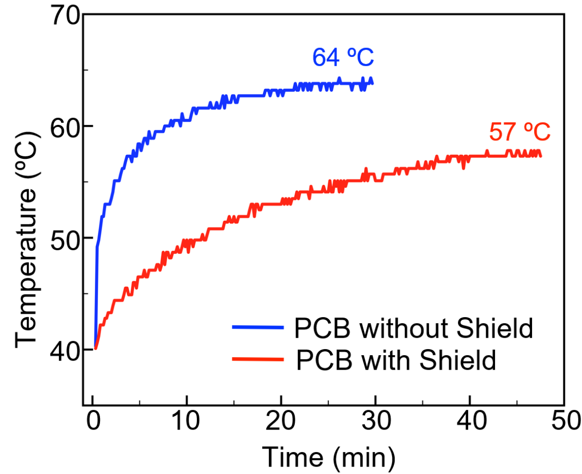

Figure 14. The CPU junction temperature of Raspberry PI with and without the shield. *A 7 °C temperature reduction was observed with the shield installed.*

It is also worth noticing that although the doping of carbon fiber and copper particles increases the electrical conductivity of the FRPC, the Raspberry PI worked without malfunction during the test process. Additionally, a thin layer of base PU or a non-conductive Thermal Interface Material (TIM) can be deployed between the electronics and the FRPC to eliminate the risk of circuit shorting.

To further investigate the additional benefits of thermal management, we performed numerical heat transport modeling using the COMSOL Multiphysics software package. Raspberry PI with and without the shield was simulated with the same boundary conditions in the experiments. As shown in Figure 15, a constant temperature of 15 °C was set for the top surfaces of the ethernet port and USB ports, while all other surfaces of these ports were set as diffusive surfaces with an emissivity of 0.165 for thermal radiation. The chip consumes 2 W with diffusive surfaces with an emissivity of 0.95. The PCB surface's emissivity was set as 0.9. The radiation background temperature was set as room temperature (20 °C). For cases where Raspberry PI was covered by the prototype, all boundary conditions were set the same as those in the bare Raspberry PI case, and the FRPC layer was 3 mm in thickness with an in-plane thermal conductivity of 2.55 W/m-K and a cross-plane thermal conductivity of 1.11 W/m-K.

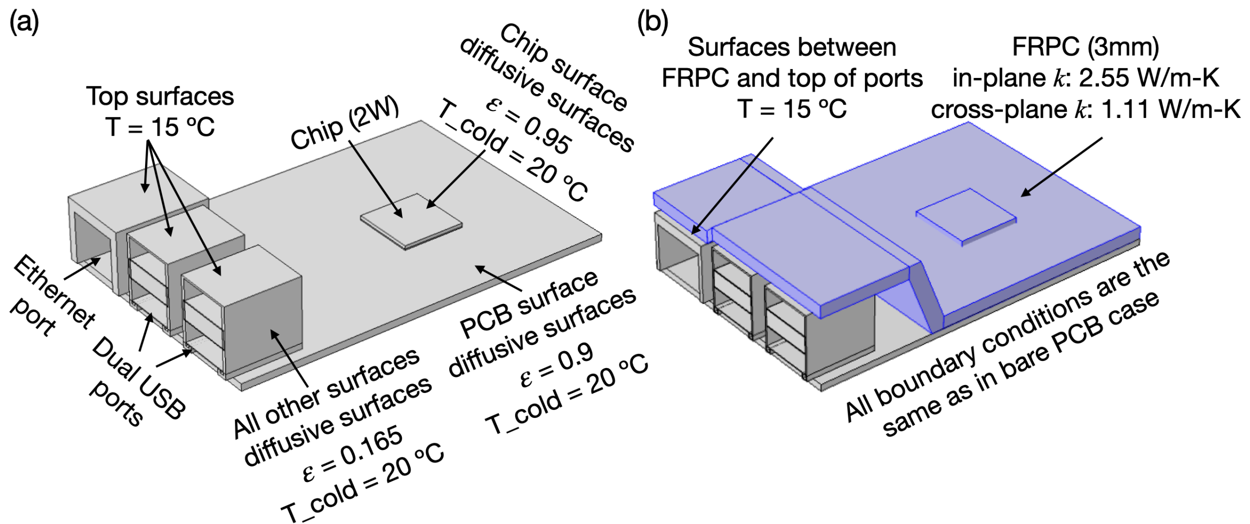

Figure 15. COMSOL modeling of the radiation shield. *Boundary conditions in COMSOL simulations for cases (a) Raspberry PI without prototype shield and (b) Raspberry PI covered by the prototype shield.*

With the boundary conditions defined, the effective thermal conductivity of the PCB and the major contact resistances were calibrated to match the experimental results. As shown in Figure 16a, b, the hot spot temperatures

for bare Raspberry PI and the one covered by the prototype were 64.4 °C and 57.4 °C, respectively, which are in excellent agreement with 64 °C and 57 °C obtained from the experiments. In this case, the cooling power at the heat sink can be reduced to achieve a lower SWaP requirements.

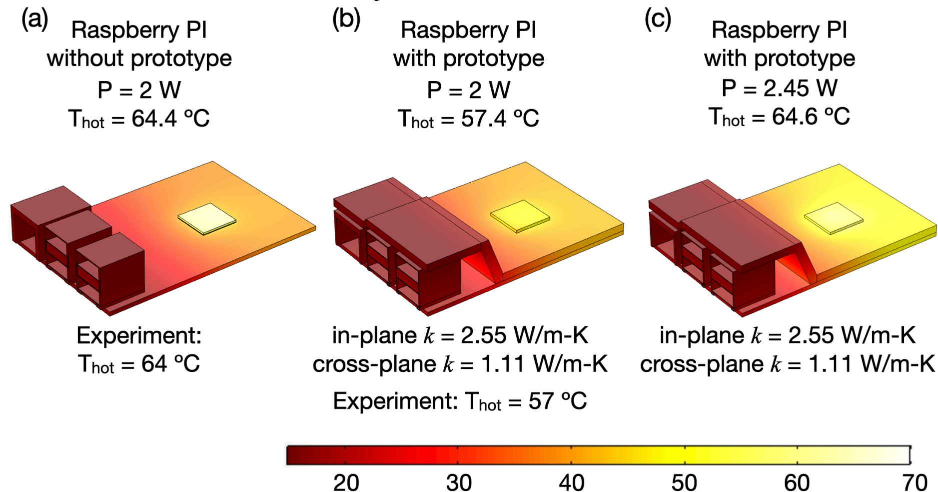

Figure 16. COMSOL simulation results. *(a) Raspberry PI was operated under vacuum without the prototype; (b) Raspberry PI was covered by the prototype shield; (c) Raspberry PI was covered by the prototype shield and was operated at higher power to reach junction temperature as high as the case in (a). Legend unit: °C.*

After the calibration, we explored the potential improvements in the power density of electronics enabled by the additional thermal budget induced by the shield. In these simulations, the chip power was increased to have the same hot spot temperature as that in the bare Raspberry PI case. As a result, with the current FRPC material, the CPU power can be increased to 2.45 W to reach 64.6 °C, representing a 22.5% increase in chip power density (Figure 16c).

IV. Conclusion

In this work, we report an FRPC layer with enhanced in-plane thermal conductivity for improved thermal management of electronics in space. The FRPC layer can share the same base polymer with the polymer composite radiation shielding layer to reduce the SWaP requirements of the radiation shielding. FRPC utilizes aligned carbon fibers in the same base polymer to achieve high in-plane thermal conductivity for electronics' heat dissipation. In addition, such a FRPC layer is manufactured by the advanced 5-axis DIW 3D printer for further improved thermal transport and structural strength. A high 2.55 W/m-K in-plane thermal conductivity, which is ~4x higher than the base polymer, was measured, and the 5-axis DIW 3D printing can achieve an >2 anisotropy between in-plane and cross-plane thermal conductivities. Additionally, testing parts manufactured using a 5-axis system have a 100% increase in stiffness and a 40% increase in peak force compared to that manufactured by conventional 3-axis printing systems. Further TVAC tests observed a 7 °C reduction in CPU temperature or a 22.5% equivalent increase in CPU power found through modeling. Future work includes comprehensive testing, including shock and vibration, outgassing, and polymer degradation over radiation dosage.

Acknowledgments

This work is supported by the U.S. Department of Energy (DoE) Small Business Innovation Research (SBIR) Program Phase I and Phase II Awards (DE-SC0022897). The authors also thank the support from the Project Managers, Maj. Adam Rich, USSF, and Cap. Chris McCartan, USAF, and the helpful discussion from Prof. Robert B. Hayes at the North Carolina State University.

References

[1]Nambiar, S. & Yeow, J. T. W., "Polymer-Composite Materials for Radiation Protection," *ACS Appl Mater Interfaces,* Vol. 4, 2012, pp. 5717, 5726.

[2]Hanson, S. C., Xiao, Y., Charrette, R. and Hayes, R. B., "A preliminary NASA compliant conformal coating for optimized space radiation shielding configurations and its mass attenuation coefficients," *Progress in Nuclear Energy,* Vol 169, 2024, pp. 105089.

[3]Dashora, P. and Gupta, G., "On the temperature dependence of the thermal conductivity of linear amorphous polymers," *Polymer (Guildf)* Vol. 37, 1996, pp. 231, 234.

[4]Lewicki, J. P. *et al.,* "3D-Printing of Meso-structurally Ordered Carbon Fiber/Polymer Composites with Unprecedented Orthotropic Physical Properties," *Scientific Reports* Vol. 7:1 No. 7, 2017, pp. 1,14.

[5]Xu, Y., Wang, X. and Hao, Q., "A mini review on thermally conductive polymers and polymer-based composites," *Composites Communications,* Vol. 24, 2021, pp. 100617.

[6]Sheng, N., Rao, Z., Zhu, C. and Habazaki, H., "Honeycomb carbon fibers strengthened composite phase change materials for superior thermal energy storage," *Appl Therm Eng*, Vol. 164, 202, pp.114493.

[7]Ma, H., Gao, B., Wang, M. and Feng, Y., "Vertical alignment of carbon fibers under magnetic field driving to enhance the thermal conductivity of silicone composites," *Polym Adv Technol,* Vol. 32, 2021, 4318–4325.

[8]Shi, S. *et al.,* "Carbon Fiber/Phenolic Composites with High Thermal Conductivity Reinforced by a Three-Dimensional Carbon Fiber Felt Network Structure." *ACS Omega,* Vol. 7, 2022, 29433–29442.

[9]Ibrahim, Y., Elkholy, A., Schofield, J. S., Melenka, G. W. and Kempers, R, "Effective thermal conductivity of 3D-printed continuous fiber polymer composites," *Advanced Manufacturing: Polymer & Composites Science,* Vol. 6, 2020, pp. 17, 28.

[10]Spoerk, M. *et al.,* "Anisotropic properties of oriented short carbon fibre filled polypropylene parts fabricated by extrusion-based additive manufacturing," *Compos Part A Appl Sci Manuf* , Vol. 113, 2018, pp. 95, 104.

[11]Yang, Y., Li, D., Si, G., Liu, Q. & Chen, Y, "Improved thermal and mechanical properties of carbon fiber filled polyamide 46 composites," *Journal of Polymer Engineering,* Vol. 37, 2017, pp. 345, 353.

[12]DeVanzo, M. & Hayes, R. B, "Ionizing radiation shielding properties of metal oxide impregnated conformal coatings," *Radiation Physics and Chemistry,* Vol. 171, 2020, 108685.